SCIENTIFIC REPORTS

OPEN

Adiabatic two-step photoexcitation effects in intermediate-band solar cells with quantum dot-in-well structure

Shigeo Asahi [ID], Toshiyuki Kaizu & Takashi Kita

We studied the dynamics of electrons generated by two-step photoexcitation in an intermediate-band solar cell (IBSC) comprising InAs/GaAs/$Al_{0.3}Ga_{0.7}$As dot-in-well (DWELL) structure using time-resolved photocurrent (TRPC) measurement. The examined IBSC exhibited considerably slower photocurrent decay than a conventional InAs/GaAs quantum dot IBSC, which is due to the extraordinarily long-lived electrons in the DWELL. In order to retrieve the electron lifetime from the decay profile, we developed a model reproducing the observed decay and performed parameter fitting. The fitting results indicate that the electron lifetime in the DWELL is approximately 30 μs. In the two-colour excitation TRPC measurement, we found that an additional infrared (IR) light accelerates the photocurrent decay while the photocurrent increases by approximately 3%, because the additional IR light causes two-step photoexcitation of electrons in the DWELLs towards the conduction band. Furthermore, we demonstrated that the open-circuit voltage increases with increasing of the contribution of the second IR excitation process.

For a high-potential candidate of the next-generation solar cells (SCs) with a high conversion efficiency, the intermediate-band solar cells (IBSCs) have drawn significant attention since the concept of IBSC was first proposed in 1997[1]. As compared to the conventional single junction SCs, whose conversion efficiency is restricted by the so-called Shockley–Queisser limit[2], the IBSC enables to dramatically reduce the transmission loss and is expected to break through the efficiency limit. For example, when an intermediate band (IB) exists in the band-gap, sub-bandgap photons can be absorbed by way of the IB. This adiabatic photo-excitation process increases photocurrent without decreasing the output voltage. Two-step photoexcitation is accomplished by two sequential optical excitations: an initial interband excitation of electrons from the valence band (VB) to the IB and following intraband excitation from the IB to the conduction band (CB). Theoretical calculation of the conversion efficiency based on the ideal detailed balance model predicts 47% under one sun and 63% under the maximum concentration of 46,200 suns[1,3]. In order to realise the IBSC attaining such a high conversion efficiency, efficient two-step photoexcitation is essential[3,4]. In particular, sufficient intraband (intersubband) excitation from the IB to the CB is crucial. Thus far, two-step photoexcitation phenomenon has been experimentally demonstrated at low temperature[5–14] and even at room temperature[15–21]. However, two-step photoexcitation at room temperature becomes weak because electrons in the IB tend to thermally escape into the CB in case the potential barrier between the IB and the CB is low[13,22–25]. Thermal electron escape pushes down quasi-Fermi level of electrons in the CB, and, therefore, lowers the output voltage. To study pure two-step photoexcitation phenomenon, many experiments have been occasionally performed at low temperature[9–11,22,26] when thermal electron escape is effectively suppressed. Detailed physics of two-step photoexcitation in InAs/GaAs quantum dot (QD) IBSCs have been clarified[6,7,9–11]. However, even at low temperature, observed two-step photocurrent is still very low. Generally, photogenerated electrons in the IB have a short lifetime of few nanoseconds due to quick recombination with holes before being excited by photons in the two-step photoexcitation process. To extend the lifetime of electrons in the IB, quantum dot superlattices[12–14] and type II quantum dots[27–30] have been proposed as possible solutions. Recently, we demonstrated that an IBSC including InAs/GaAs/$Al_{0.3}Ga_{0.7}$As dot-in-well (DWELL) structure sufficiently suppresses thermal electron escape at room temperature and attains an extremely long-lived electrons

Department of Electrical and Electronic Engineering, Graduate School of Engineering, Kobe University, Kobe, Japan. Correspondence and requests for materials should be addressed to S.A. (email: asahis@people.kobe-u.ac.jp)
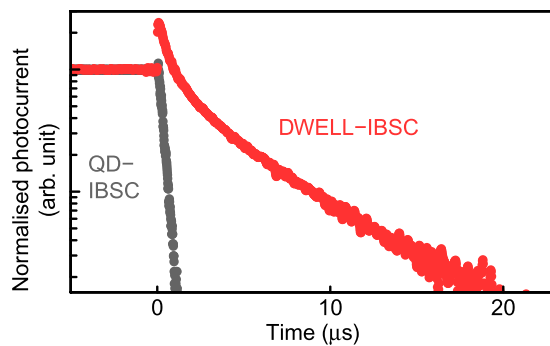
1

Figure 1. Normalised photocurrent decay profiles for the DWELL-IBSC (red circles) and reference QD-IBSC (black circles) at 300 K.

in the DWELL because photogenerated holes are thermally pumped out[16]. This SC is called DWELL-IBSC which achieves efficient two-step photocurrent generation even at room temperature. The external quantum efficiency spectrum of DWELL-IBSC obviously show an enhancement caused by the two-step photocurrent above a threshold wavelength of 930 nm corresponding to the fundamental absorption edge of the InAs wetting layer[16]. In addition, we have investigated the detailed two-step photocurrent generation as functions of the excitation power in interband and intersubband transitions. The two-step photocurrent exhibited saturation when the interband excitation power increased, and the saturation level depended on the intersubband excitation power[19]. We proposed a model to interpret the observed two-step photocurrent and discussed the dynamics of electrons generated in the DWELL. Besides, the simulation results suggested that the electron lifetime in the DWELL has been estimated to be in a range from 400 μs to 2 ms[19], which is extremely long as compared to the value of conventional InAs/GaAs QDs[31]. In this study, we performed time-resolved photocurrent (TRPC) measurement to directly investigate the electron dynamics with the long lifetime in the DWELL-IBSC. We confirmed an extremely slow response of the photocurrent decay in the DWELL-IBSC. The additional infrared (IR) light irradiation in the two-colour photoexcitation process dramatically accelerates the TRPC decay and recovers the open-circuit voltage.

Results

Figure 1 shows the typical TRPC decay profiles for the DWELL-IBSC and the reference QD-IBSC. Each excitation power density was 3.7 W/cm² for the DWELL-IBSC and 0.21 W/cm² for the reference QD-IBSC, respectively. We detected spike-like signals in the both decay profiles for the DWELL-IBSC and QD-IBSC where the amplitude of the spikes was 0.18 mA/cm². These signal arises from an impedance mismatch between the SCs and the current amplifier. As the spike signal appeared at the very initial stage that we did not focus at, we neglected it in our analysis. For the reference QD-IBSC, the photocurrent rapidly decreases and exhibits a single exponentially decaying curve just after stopping the excitation. The photogenerated electrons in the intermediate states are promptly extracted by thermal escape process because of the relatively shallow confinement energy at room temperature. The estimated decay time is approximately 250 ns, which is predominantly determined by the RC time constant. The estimated junction capacitance of QD-IBSC is 4 nF[32], and the RC time constant of the SC is estimated to be 200 ns. Conversely, the DWELL-IBSC exhibits a slow, stretched-exponential decay profile. The potential barrier of $Al_{0.3}Ga_{0.7}As$ is high enough to suppress thermal electron escape even at room temperature, though photogenerated holes are thermally pumped towards the p-electrode due to the relatively low barrier height. That causes electron–hole separation, and, therefore, the electron lifetime in the DWELLs is extended. This electron–hole separation was also confirmed by the temperature dependence of the photoluminescence intensity of the DWELL-IBSC[19]. Despite the strong confinement of electrons, they gradually escape in the thermal process, resulting in a very slow and stretched-exponential decay profile. Thus, we directly observed the extraordinarily long-lived electrons in the DWELLs by using the TRPC measurement technique.

In order to retrieve the electron lifetime from the decay profile, we propose a model reproducing the decay curve. In this model, we neglected dynamics contributed by holes because of quick thermal escape from the DWELL. Figure 2(a) illustrates the model of the CB lineup. The rate equation representing the electron density per unit area in the ith DWELL, n_i, is given by

$$\frac{\mathrm{d}n_i}{\mathrm{d}t} = sG_{784\,\mathrm{nm},i} - \frac{n_i}{\tau_A} - \frac{n_i}{\tau_{th}} + \gamma N_{i-1},$$

(1)

where $G_{784\,\mathrm{nm},i}$ is the interband photocarrier generation rate in the ith DWELL per unit area, τ_A and τ_{th} are the annihilation time and thermal escape time in the DWELL, respectively. N_{i-1} is the generated areal density of electrons supplied from the $(i-1)$th DWELL per unit time and is defined as follows:

$$N_{i-1} = \frac{n_{i-1}}{\tau_{th}} + (1 - \gamma)N_{i-2}.$$

(2)

γ is the fraction of electrons trapped into the ith DWELL. s is the fraction of long-lived electrons in the DWELL owing to the electron–hole separation. Part of electrons in the DWELL quickly recombines with holes within few
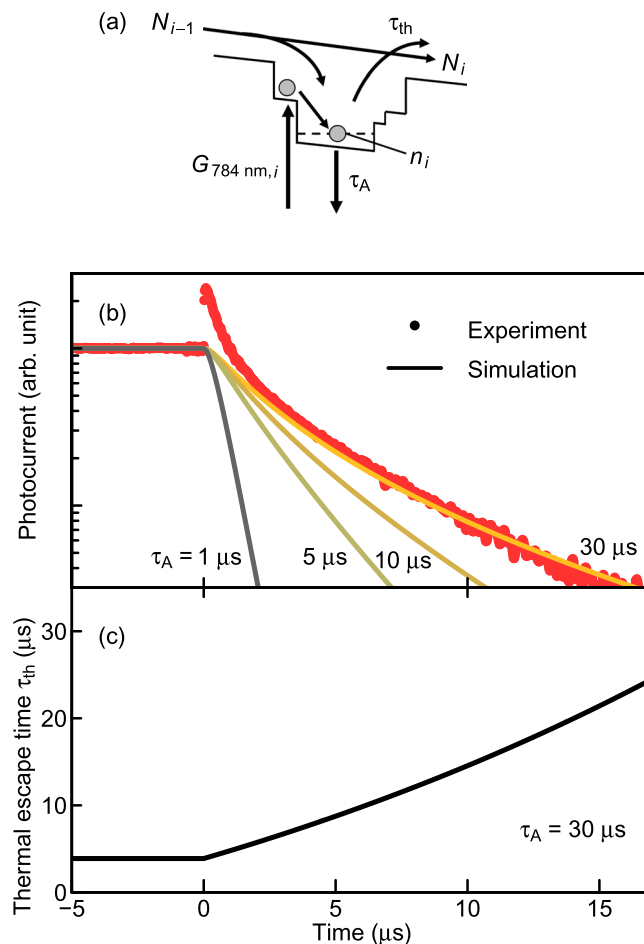
Figure 2. Calculated result of TRPC decay of DWELL-IBSC. (**a**) Schematic numerical model of photocurrent decay profile in the DWELL-IBSC. (**b**) Calculated results of photocurrent decay (solid line). The red circles indicate the observed decay curve for the DWELL-IBSC shown in Fig. 1. (**c**) Calculated thermal escape τ_{th}. The annihilation time used in the calculation is 30 μs.

nanoseconds, and the remaining electrons slowly decay in the thermal escape process. Thus, $sG_{784\,nm,i}$ corresponds to the generation rate of long-lived electrons. $sG_{784\,nm,i}$ becomes zero after stopping the irradiation of the LD ($t > 0$). The second and third terms on the right-hand side of Eq. (1) represent the annihilation rate in the DEWLL and the thermal escape rate of electrons, respectively. The electrons separated from holes can be alive much longer than the radiative recombination time. The annihilation time of electrons is, therefore, mainly determined by the Shockley–Read–Hall recombination and is expected to extend the lifetime into a temporal region of microseconds ~ milliseconds. We assumed that thermally extracted electrons immediately reach the next DWELL because the estimated drifting time through the 50-nm-thick $Al_{0.3}Ga_{0.7}As$ barrier is less than one picosecond, which is negligible as compared to the temporal scale of interest. For simplicity, we neglected band bending due to electron accumulation in DWELLs and nonlinear effect such as Auger effect. In addition, we used same s and γ values (0.01 and 0.08) for all DWELL-layers in Eq. (1). It should be noted that Eq. (1) presents an electron balance model in one DWELL-layer, and the unit of n_i is m^{-2}. $G_{784\,nm,i}$ is obtained by using the Beer–Lambert law as follows

$$G_{784\,nm,i} = P_{784\,nm,i}\left\{1 - \exp\left[-\left(1 - f_{well,i}\right)\alpha_{well}d_{well}\right]\right\},\tag{3}$$

where $P_{784\,nm,i}$ is the incident photon flux of the 784-nm LD light source at the ith DWELL, $f_{well,i}$ is the electron occupation factor of the GaAs QW states in the ith DWELL, α_{well} is the interband absorption coefficient of the QW, and the QW thickness d_{well} is 16 nm. $P_{784\,nm,i}$ is calculated from the excitation power density considering the reflectivity of the SC surface and the photon energy. We considered that the 784-nm LD excites the fundamental states of the GaAs QW. The state filling effect is also taken into account in Eq. (3). We used 3,000 cm^{-1} for α_{well}[33]. The quasi-Fermi level of electrons in the DWELL is described using the Fermi–Dirac distribution

$$f_{well,i} = \frac{1}{1 + \exp[(E_{well} - E_{f,i})/kT]} \approx \exp\left(\frac{E_{f,i} - E_{well}}{kT}\right),\tag{4}$$
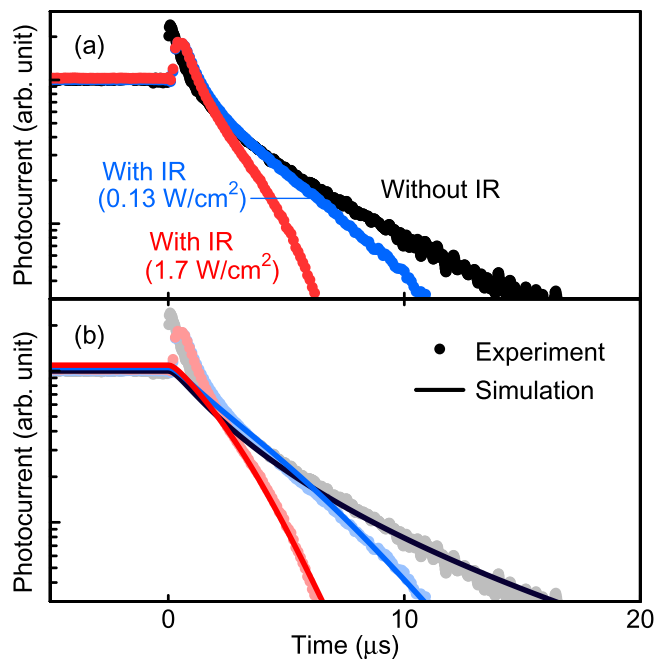
Figure 3. Photocurrent decay profiles with additional IR light. (**a**) Photocurrent decay profiles for the DWELL-IBSC with different power densities of the additional IR light. (**b**) Calculated results of the photocurrent decay profiles with the additional IR light.

where E_{well} is the electron energy level of the fundamental state of the GaAs QW, k is the Boltzmann constant, T is the temperature (300 K), and $E_{f,i}$ is the quasi-Fermi level of the electrons of the ith DWELL. Here, we used the Boltzmann approximation in Eq. (4) because $E_{f,i}$ is sufficiently lower than E_{well}. $E_{f,i}$ can be expressed as follows

$$E_{f,i} = E_{equil,i} + kT \ln\left(\frac{n_i}{n_{intr,i}}\right), \tag{5}$$

where $E_{equil,i}$ is the Fermi-level in the state of thermal equilibrium and $n_{intr,i}$ is the intrinsic areal electron density in the ith DWELL. To calculate τ_{th}, we used the thermionic emission model of QWs described as[34,35]

$$\tau_{th} = d_{well}\sqrt{\frac{2\pi m^*}{kT}} \exp\left(\frac{E_{AlGaAs} - E_{f,i}}{kT}\right), \tag{6}$$

where m^* is the effective electron mass and E_{AlGaAs} is the CB edge of $Al_{0.3}Ga_{0.7}As$. We used 6.1×10^{-32} kg for m^*. We substituted Eqs (2–6) into Eq. (1), and, then, numerically calculated n_i in ith DWELL. Thereby, the calculated short-circuit current density, J_{sc}, was obtained from following equations

$$J_{sc} = qN_{10}, \tag{7}$$

where q is the elementary charge.

Solid lines in Fig. 2(b) indicate numerically calculated TRPC decay profiles for the DWELL-IBSC at different τ_A's. With the increase of τ_A, the calculated decay approaches the experimental results. According to a curve fitting to reproduce the observed decay curve, τ_A is estimated to be 30 μs. Figure 2(c) shows the calculated τ_{th} at τ_A of 30 μs. τ_{th} is a few microseconds during the excitation and exhibits a monotonic increase after stopping the excitation. Since τ_{th} is smaller than τ_A at time < 20 μs, the decay of DWELL-IBSC shown in Fig. (1) is predominantly determined by τ_{th}. The estimated τ_A becomes smaller than the value obtained by a systematic excitation power dependence of the two-step photocurrent, which is in the range from 400 μs to 2 ms[19]. τ_A evaluated by the TRPC measurements in this work is believe to be more precise rather than the value predicted by the analysis of carrier dynamics based on data measured at the steady state condition.

Subsequently, we performed two-colour excitation TRPC measurements for the DWELL-IBSC to investigate the temporal behaviour when irradiated by IR light at 300 K. Figure 3(a) shows the results. In this experiment, we used a supercontinuum white laser light passing through a long pass filter transmitting IR light above 1,250 nm. The fundamental transition energy of QDs in the DWELL-IBSC is 1.05 eV (1,180 nm) at 300 K so that the additional IR light only excites the states in the intraband of the DWELLs[16]. We confirmed that the observed photocurrent obeys linear relationship with the IR photon density, indicating non-linear phenomenon such as two-phonon absorption does not occur in this measurement. The first interband excitation light used and its power density were the same as those in the experiment shown in Fig. 1. It is noted that the photocurrent profiles shown in Fig. 3(a) are un-normalised, original data. We found that the additional IR light accelerates the photocurrent decay while the photocurrent increases by ~3% at the IR power density of 1.7 W/cm². The additional
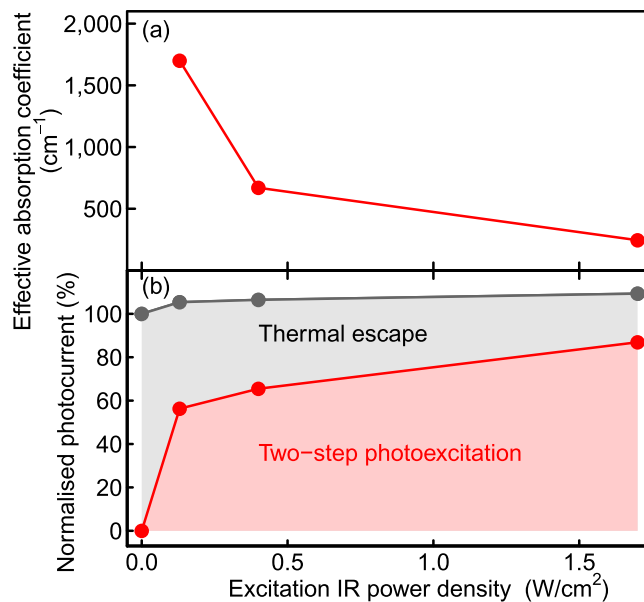
Figure 4. Retrieved fitting values from the simulation. (**a**) Intraband absorption coefficient of intraband excitation for InAs QD as a function of excitation IR power density. (**b**) Calculated cause of the photocurrent which is normalised by the photocurrent without IR excitation.

IR light causes two-step photoexcitation of electrons in the DWELLs, resulting in this fast decay profile. In order to interpret the decay profile under the irradiation of the additional IR light, we took into account the term of two-step photocurrent generation rate, $G_{\text{IR},i}$, in Eq. (1) as follows

$$\frac{\mathrm{d}n_i}{\mathrm{d}t} = sG_{784\,\text{nm},i} - \frac{n_i}{\tau_\text{r}} - \frac{n_i}{\tau_\text{th}} + \gamma N_{i-1} - G_{\text{IR},i}. \tag{8}$$

$G_{\text{IR},i}$ can be expressed as

$$G_{\text{IR},i} = P_{\text{IR},i}\Big[1 - \exp\Big(-f_{\text{dot},i}\,\alpha_{\text{dot}}d_{\text{dot}}\Big)\Big], \tag{9}$$

where $P_{\text{IR},i}$ is the incident photon flux of the IR light, $f_{\text{dot},i}$ is the *effective* occupation factor at the QD states in the ith DWELL, α_{dot} is the *effective* absorption coefficient of InAs QD, and the InAs QD layer thickness d_{dot} is 4 nm. We considered that the intraband transition does not occur in the QW states and only occurs in the QD states, because the optical dipole transition for the intraband transition in quantum structures is only allowed for the component polarized parallel to the confined direction[36]. Here, it is noted that, in our model as illustrated in Fig. 2(a), we simply assumed a single electron energy level as the initial state in InAs QD. However, according to the PL measurements[16], at least three quantized states play the role of the initial state. Therefore, $f_{\text{dot},i}$ is the *effective* occupation factor for the initial state containing several quantized states in QDs, and α_{dot} is the *effective* absorption coefficient for the initial state. We assumed that two-step photoexcitation occurs at the fundamental and excited states of QDs. $f_{\text{dot},i}$ can be calculated as

$$f_{\text{dot},i} = \frac{1}{1 + \exp[(E_{\text{dot}} - E_{\text{f},i})/kT]}, \tag{10}$$

where E_{dot} is the electron energy level of InAs QD. We assume that the states of GaAs QW and InAs QD are thermally coupled and used the same value for $E_{\text{f},i}$ in Eqs (4 and 10). Figure 3(b) summarises the calculation results. The calculation results agree well with the experimental data and reproduce that the additional IR light accelerates the photocurrent decay. We found that the intraband effective absorption coefficient of InAs QD α_{dot} changes as a function of excitation intensity. The best fit α_{dot} values are summarised in Fig. 4(a). α_{dot} decreases with excitation IR power density. As the additional IR light increases, the quasi-Fermi level of DWELL falls, and the probability of intraband excitation decreases, leading to the decrease in α_{dot} with the IR power density. The evaluated intraband absorption coefficient is in the range of 200–1,800 cm^{-1}, which is comparable to the reported values[7,37]. By distinguishing the current of thermal escape and two-step photoexcitation, we evaluated the amount of the photocurrent caused by the additional IR light illumination. The estimated result is drawn in Fig 4(b). Without the additional IR light, photocurrent is only caused by thermal electron escape. In contrast, when irradiated by the additional IR light, electrons are also extracted by two-step photoexcitation. Two-step photocurrent increases as the power density of the additional IR light increases. Conversely, as electrons are extracted by the additional IR light irradiation, the electron density in the DWELL decreases and the contribution of the thermal electron escape decreases for that. As the detected photocurrent is a sum of the decreased thermally escaped current and the increased two-step photocurrent, the change in the detected photocurrent by the additional IR light is small.
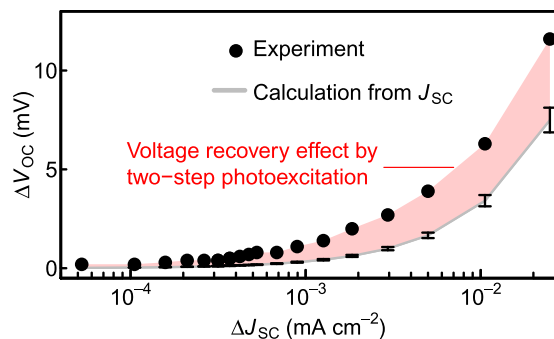
Figure 5. Change in the open-circuit voltage (ΔV_{OC}) as a function of the change in the short-circuit current (ΔJ_{SC}) under the irradiation of the additional IR light measured at 300 K. The grey line indicates ΔV_{OC} estimated from experimentally observed short-circuit current (J_{SC}) using Eq. (11). The errors represent uncertainty for diode factor n of 1.2 ± 0.1, which is determined from the slope of dark Log J–V curve. The red area is the difference between the experimental observation and the estimation ΔV_{OC}, interpreted as the voltage recovery by the two-step photoexcitation.

When the power density of the additional IR light was 1.7 W/cm^2, ~80% of the detected photocurrent is caused by the two-step photocarrier generation.

When only irradiated by the 784-nm LD, quasi-Fermi level is single. When the additional IR light pumps electrons from the IB into the CB, quasi-Fermi levels of the IB and the CB start splitting, and, therefore, the adiabatic process of the two-step photoexcitation recovers the output voltage[38]. In order to demonstrate the voltage recovery effect caused by two-step photoexcitation, we investigated short-circuit current, J_{SC}, and open-circuit voltage, V_{OC}, under the irradiation of the both sources, the 784-nm LD and the additional IR light. The solid circles in Fig. 5 show the measured ΔV_{OC} as a function of ΔJ_{SC}. Here, ΔJ_{SC} and ΔV_{OC} are the changes in J_{SC} and V_{OC} caused by the additional IR light irradiation, respectively. In this measurement, the power density of 784-nm LD was 3.7 W/cm^2, and the power density of the additional IR light was in the range from 58 mW/cm^2 to 11 W/cm^2. ΔV_{OC} dramatically increases with ΔJ_{SC}.

Discussion

Both the photocurrent increase and the voltage recovery caused by the quasi-Fermi level splitting contribute to ΔV_{OC}. ΔJ_{SC} itself increases V_{OC}. In order to visualise the voltage recovery effect, we compare the experimentally observed ΔV_{OC} with ΔV_{OC} intrinsically expected to be caused by ΔJ_{SC}. According to the detailed balance model for the ideal single junction SC, the relationship between J_{SC} and V_{OC} obeys the following equation

$$V_{oc} = \frac{nkT}{q} \ln\left(\frac{J_{sc}}{J_0} + 1\right),$$

(11)

where n is diode quality factor, J_0 is saturation current density. First, we substituted measured V_{OC} and J_{SC} under the irradiation of the 784-nm LD only into Eq. (11) and obtained J_0 of 3.7×10^{-2} mA/cm^2. Here, we used 1.2 ± 0.1 for n, which is determined from the slope of dark Log J–V curve of the DWELL-IBSC. Utilising J_0, we calculated V_{OC} by substituting J_{SC} measured when irradiated by the IR light into Eq. (11). The calculated results are depicted by the grey solid line in Fig. 5. The experimentally observed ΔV_{OC} apparently surpasses the values increased by ΔJ_{SC}, and the difference indicated by the red area in Fig. 5 in between them corresponds to the voltage recovery caused by the quasi-Fermi level splitting. It demonstrates the principle concept of the two-step photocarrier generation in IBSC in which total photocurrent increases without decreasing of the photovoltage.

Methods

Solar cell fabrication. An Al$_{0.3}$Ga$_{0.7}$As p–i–n SC device structure was fabricated on an n^+-type GaAs (001) substrate by using solid-source molecular beam epitaxy. An n-Al$_{0.3}$Ga$_{0.7}$As (700 nm)/n^+-Al$_{0.3}$Ga$_{0.7}$As (150 nm) layer was deposited on a 400-nm-thick n^+-GaAs buffer layer. Subsequently, a 1400-nm-thick i-layer including a DWELL structure was deposited. The i-layer consisted of Al$_{0.3}$Ga$_{0.7}$As (540 nm), ten periods of GaAs (10 nm)/ InAs QDs (two monolayers)/GaAs (6 nm)/Al$_{0.3}$Ga$_{0.7}$As (50 nm), and Al$_{0.3}$Ga$_{0.7}$As (200 nm) layers. Finally, a 150-nm-thick p-Al$_{0.3}$Ga$_{0.7}$As emitter layer was grown. The detailed SC structure and its band diagram have been reported in our previous publications[16,19]. In addition, we also fabricated a conventional InAs/GaAs QD-IBSC with the same i-layer thickness and ten QD layers as a reference IBSC.

TRPC measurement. In order to elucidate the dynamics of photogenerated electrons in the DWELLs, we performed TRPC measurement for the two IBSCs. Two laser diodes (LDs) with different wavelengths were used for exciting the SCs; a 784-nm LD was used for the DWELL-IBSC, and a 940-nm LD was used for the reference QD-IBSC. Both LDs excited the intermediate state[16]. The LD output power was directly modulated by a function generator that outputs a square-wave signal with a frequency of 100 Hz and a duty ratio of 50%. We detected short-circuit photocurrent by using a current amplifier and a digital oscilloscope triggered by the function generator. The temporal response time of the detection system was ~20 ns, which is sufficiently fast to investigate the electron dynamics in the SCs. All measurements were conducted at 300 K.

Theoretical simulation.   We performed calculations using Visual Studio Community 2017. The programming language used was Visual C++.

Data Availability
The data that support the findings of this study are available from the corresponding author upon request.

Code Availability
The computer code used in this study are available from the corresponding author upon request.

References
1. Luque, A. & Martí, A. Increasing the efficiency of ideal solar cells by photon induced transitions at intermediate levels. *Phys. Rev. Lett.* **78**, 5014–5017 (1997).
2. Shockley, W. & Queisser, H. J. Detailed Balance Limit of Efficiency of p-n Junction Solar Cells. *J. Appl. Phys.* **32**, 510–519 (1961).
3. Okada, Y. *et al.* Intermediate band solar cells: Recent progress and future directions. Appl. *Phys. Rev.* **2**, 021302 (2015).
4. Luque, A., Martí, A. & Stanley, C. Understanding intermediate-band solar cells. *Nat. Photonics* **6**, 146–152 (2012).
5. Martí, A. *et al.* Production of photocurrent due to intermediate-to-conduction-band transitions: A demonstration of a key operating principle of the intermediate-band solar cell. *Phys. Rev. Lett.* **97**, 247701 (2006).
6. Kita, T., Maeda, T. & Harada, Y. Carrier dynamics of the intermediate state in InAs/GaAs quantum dots coupled in a photonic cavity under two-photon excitation. *Phys. Rev. B* **86**, 035301 (2012).
7. Harada, Y., Maeda, T. & Kita, T. Intraband carrier dynamics in InAs/GaAs quantum dots stimulated by bound-to-continuum excitation. *J. Appl. Phys.* **113**, 223511 (2013).
8. Shoji, Y., Akimoto, K. & Okada, Y. Self-organized InGaAs/GaAs quantum dot arrays for use in high-efficiency intermediate-band solar cells. *J. Phys. D. Appl. Phys.* **46**, 24002 (2013).
9. Tamaki, R., Shoji, Y., Naitoh, S., Okada, Y. & Miyano, K. Extreme broadband photocurrent spectroscopy on InAs quantum dot solar cells. *Proc. SPIE* **9358**, 93580V (2015).
10. Tamaki, R., Shoji, Y., Okada, Y. & Miyano, K. Spectrally resolved intraband transitions on two-step photon absorption in InGaAs/GaAs quantum dot solar cell. *Appl. Phys. Lett.* **105**, 073118 (2014).
11. Tanibuchi, T. *et al.* Photocarrier transport dynamics in InAs/GaAs quantum dot superlattice solar cells using time-of-flight spectroscopy. *Phys. Rev. B* **94**, 195313 (2016).
12. Kada, T. *et al.* Two-step photon absorption in InAs/GaAs quantum-dot superlattice solar cells. *Phys. Rev. B* **91**, 201303-1–201303-6 (2015).
13. Watanabe, S. *et al.* Two-step photocurrent generation enhanced by miniband formation in InAs/GaAs quantum dot superlattice intermediate-band solar cells. *Appl. Phys. Lett.* **110**, 193104 (2017).
14. Kada, T. *et al.* Efficient two-step photocarrier generation in bias-controlled InAs/GaAs quantum dot superlattice intermediate-band solar cells. *Sci. Rep.* **7**, 5865 (2017).
15. Okada, Y. *et al.* Increase in photocurrent by optical transitions via intermediate quantum states in direct-doped InAs/GaNAs strain-compensated quantum dot solar cell. *J. Appl. Phys.* **109**, 024301 (2011).
16. Asahi, S. *et al.* Suppression of thermal carrier escape and efficient photo-carrier generation by two-step photon absorption in InAs quantum dot intermediate-band solar cells using a dot-in-well structure. *J. Appl. Phys.* **116**, 063510-1–063510-5 (2014).
17. Sellers, D. G., Polly, S., Hubbard, S. M. & Doty, M. F. Analyzing carrier escape mechanisms in InAs/GaAs quantum dot p-i-n junction photovoltaic cells. *Appl. Phys. Lett.* **104**, 223903 (2014).
18. Elborg, M. *et al.* Voltage dependence of two-step photocurrent generation in quantum dot intermediate band solar cells. *Sol. Energy Mater. Sol. Cells* **134**, 108–113 (2014).
19. Asahi, S. *et al.* Saturable Two-Step Photocurrent Generation in Intermediate-Band Solar Cells Including InAs Quantum Dots Embedded in Al0.3Ga0.7As/GaAs Quantum Wells. *IEEE J. Photovoltaics* **6**, 465–472 (2016).
20. Ning, Z. *et al.* Quantum-dot-in-perovskite solids. *Nature* **523**, 324–328 (2015).
21. Hosokawa, H. *et al.* Solution-processed intermediate-band solar cells with lead sulfide quantum dots and lead halide perovskites. *Nat. Commun.* **10**, 43 (2019).
22. Tex, D. M., Kamiya, I. & Kanemitsu, Y. Control of hot-carrier relaxation for realizing ideal quantum-dot intermediate-band solar cells. *Sci. Rep.* **4**, 4125 (2014).
23. Shoji, Y., Oshima, R., Takata, A., Morioka, T. & Okada, Y. Multi-stacked InGaAs/GaNAs quantum dot solar cell fabricated on GaAs (311)B substrate. *Conf. Rec. IEEE Photovolt. Spec. Conf.* **112**, 1859–1862 (2010).
24. Antolín, E. *et al.* Reducing carrier escape in the InAs/GaAs quantum dot intermediate band solar cell. *J. Appl. Phys.* **108**, 064513 (2010).
25. Jolley, G., Fu, L., Lu, H. F., Tan, H. H. & Jagadish, C. The role of intersubband optical transitions on the electrical properties of InGaAs/GaAs quantum dot solar cells. *Prog. Photovoltaics Res. Appl.* **21**, 736–746 (2012).
26. Nozawa, T., Takagi, H., Watanabe, K. & Arakawa, Y. Direct Observation of Two-Step Photon Absorption in an InAs/GaAs Single Quantum Dot for the Operation of Intermediate-Band Solar Cells. *Nano Lett.* **15**, 4483–4487 (2015).
27. Shoji, Y., Tamaki, R. & Okada, Y. Multi-stacked GaSb/GaAs type-II quantum nanostructures for application to intermediate band solar cells. *AIP Adv.* **7**, 065305 (2017).
28. Tayagaki, T. & Sugaya, T. Type-II InP quantum dots in wide-bandgap InGaP host for intermediate-band solar cells. *Appl. Phys. Lett.* **108**, 153901 (2016).
29. Hwang, J. *et al.* Multiphoton Sub-Band-Gap Photoconductivity and Critical Transition Temperature in Type-II GaSb Quantum-Dot Intermediate-Band Solar Cells. *Phys. Rev. Appl.* **1**, 051003 (2014).
30. Sato, D. *et al.* Extremely long carrier lifetime at intermediate states in wall-inserted type II quantum dot absorbers. *J. Appl. Phys.* **112**, 094305 (2012).
31. Harbord, E., Spencer, P., Clarke, E. & Murray, R. The influence of size distribution on the luminescence decay from excited states of InAs/GaAs self-assembled quantum dots. *J. Appl. Phys.* **105**, 033507 (2009).
32. Sze, S. M. Bipolar devices. in Physics of semiconductor devices (John Wiley & Suns, Inc.).
33. Miller, D. A. B. Large room-temperature optical nonlinearity in GaAs/Ga1−x AlxAs multiple quantum well structures. *Appl. Phys. Lett.* **41**, 679 (1982).
34. Schneider, H. & Klitzing, K. V. Thermionic emission and Gaussian transport of holes in a GaAs/AlxGa1-xAs multiple-quantum-well structure. *Phys. Rev. B* **38**, 6160–6165 (1988).
35. Aihara, T. *et al.* Effect of number of stack on the thermal escape and non-radiative and radiative recombinations of photoexcited carriers in strain-balanced InGaAs/GaAsP multiple quantum-well-inserted solar cells. *J. Appl. Phys.* **117**, 084307 (2015).
36. Harrison, P. Carrier-photon scattering. in Quantum wells, wires and dots 332–338 (John Wiley & Suns, Inc., 2005).
37. Luque, A. *et al.* Absorption coefficient for the intraband transitions in quantum dot materials. *Prog. Photovolt Res. Appl.* **21**, 658–667 (2013).
38. Ramiro, I. *et al.* Analysis of the intermediate-band absorption properties of type-II GaSb/GaAs quantum-dot photovoltaics. *Phys. Rev. B* **96**, 125422 (2017).

Author Contributions

S.A. wrote the manuscript, carried out experiments, and performed theoretical calculation; T. Kaizu designed and fabricated the solar cell devices; T. Kita co-wrote the manuscript and was in charge of overall direction and planning.

Additional Information

Competing Interests: The authors declare no competing interests.

Publisher's note: Springer Nature remains neutral with regard to jurisdictional claims in published maps and institutional affiliations.